Science Advances
AAAS
advances.sciencemag.org/cgi/content/full/4/4/eaas8925/DC1

Supplementary Materials for

Ultralight and fire-resistant ceramic nanofibrous aerogels with temperature-invariant superelasticity

Yang Si, Xueqin Wang, Lvye Dou, Jianyong Yu, Bin Ding

Published 27 April 2018, *Sci. Adv.* **4**, eaas8925 (2018)
DOI: 10.1126/sciadv.aas8925

The PDF file includes:

- Supplementary Discussions

Other Supplementary Material for this manuscript includes the following:
(available at advances.sciencemag.org/cgi/content/full/4/4/eaas8925/DC1)

- movie S1 (.mp4 format). Compression and recovery processes of CNFAs.
- movie S2 (.mov format). Fast recovery of CNFAs by rebounding a steel ball.
- movie S3 (.mp4 format). Compression testing in the flame of an alcohol lamp.
- movie S4 (.mp4 format). Compression testing in the flame of a butane blowtorch.

Supplementary Materials

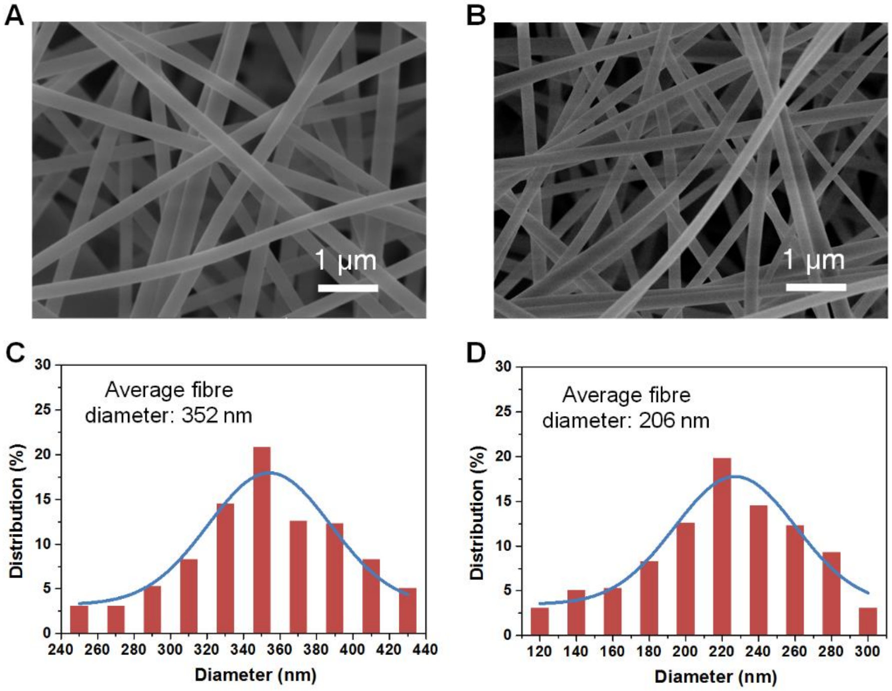

fig. S1. Fabrication of electrospun SiO$_2$ nanofibers. SEM images of (**A**) PVA/TEOS as-spun nanofibers and (**B**) SiO$_2$ nanofibers. Histogram demonstrating the fiber diameter distribution of (**C**) PVA/TEOS as-spun nanofibers and (**D**) SiO$_2$ nanofibers.

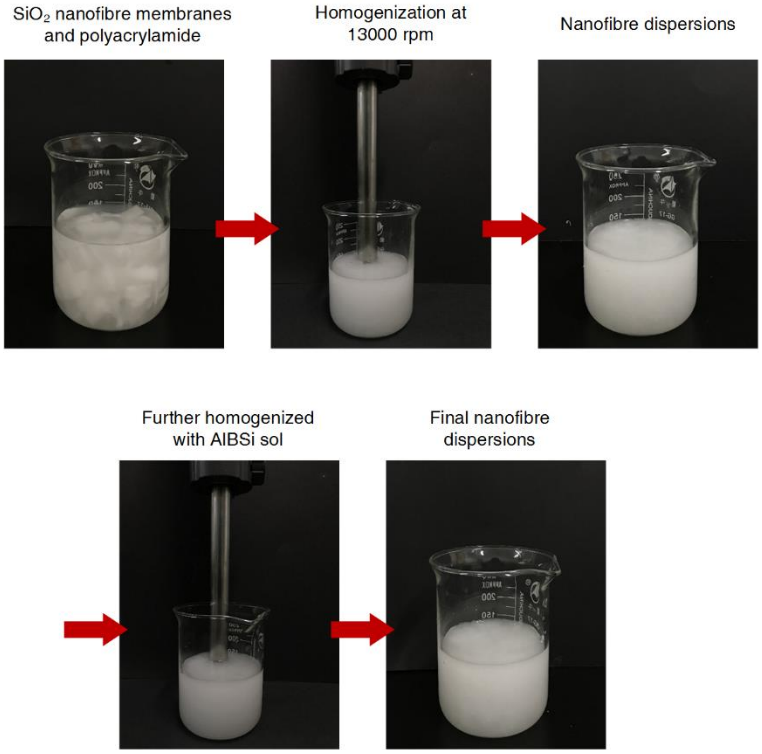

fig. S2. Homogenization of nanofibers. Optical photographs showing the preparation of AlBSi/polyacrylamide/SiO_2 nanofiber dispersions by high-speed homogenization at 13000 rpm.

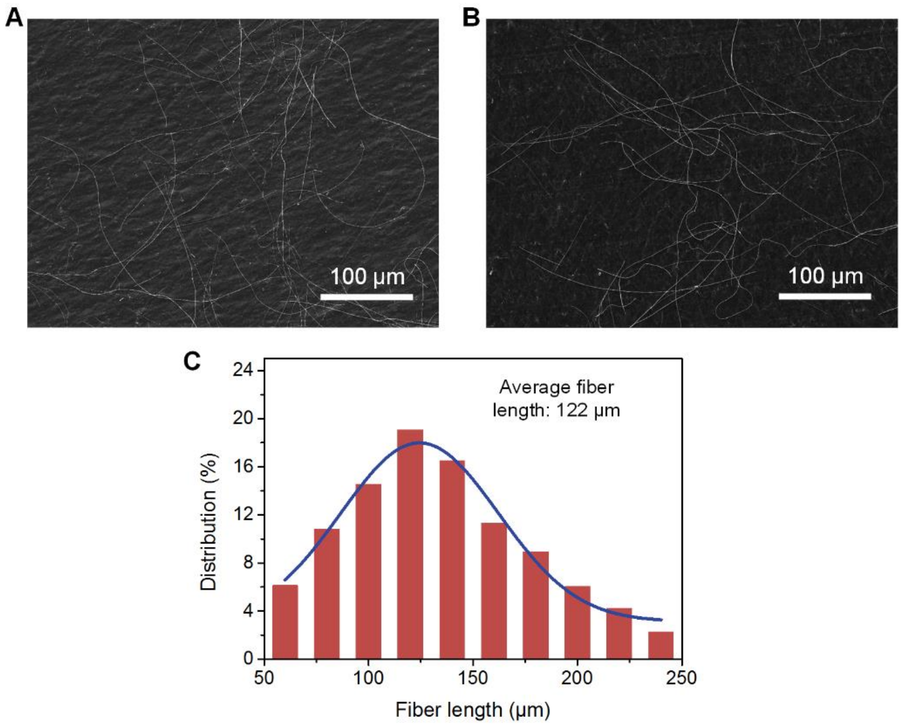

fig. S3. Morphology of homogenized nanofibers. (**A**) and (**B**) SEM images of the homogenized nanofibers. (**C**) Histogram showing the fiber length distribution of the homogenized nanofibers.

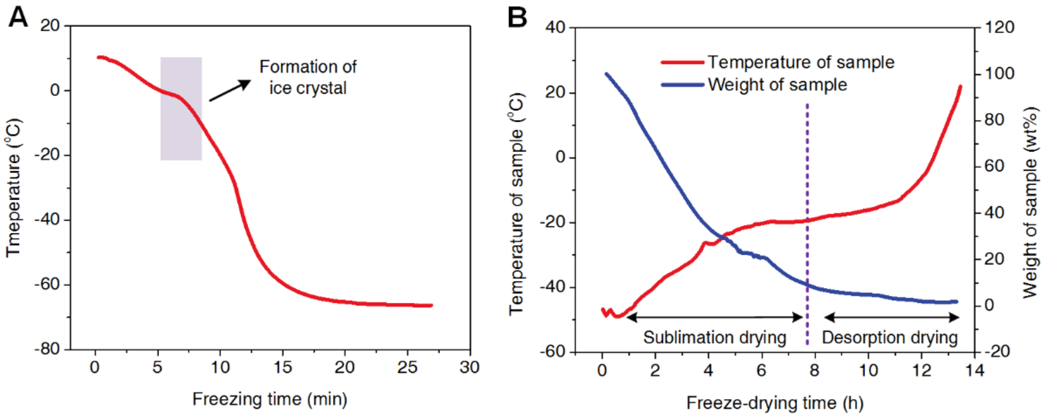

fig. S4. The freezing of nanofiber dispersions. (**A**) The temperature of the nanofiber dispersions versus freezing time. (**B**) The temperature and weight of the frozen nanofiber sample with increasing freeze-drying time.

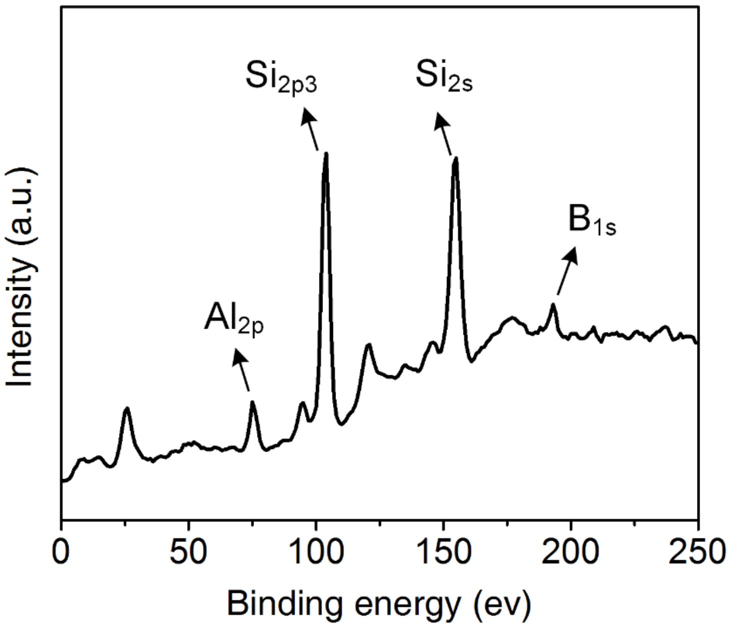

fig. S5. Magnified XPS spectrum. XPS spectrum of CNFAs with the binding energy ranging from 0 to 250 eV.

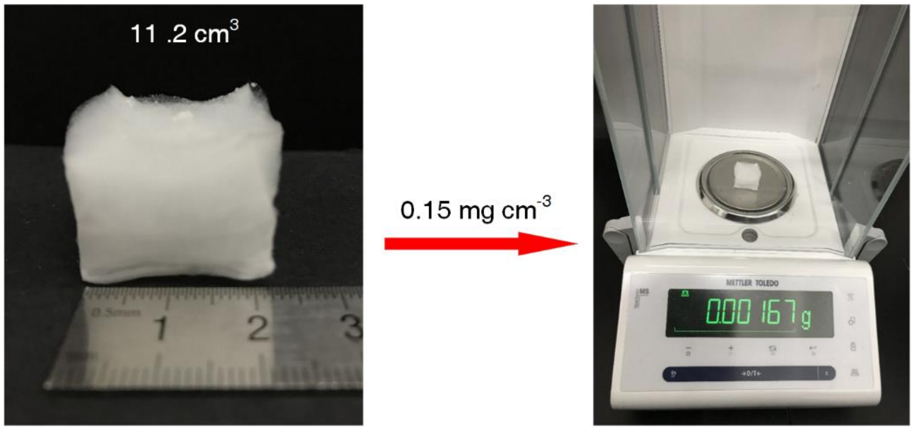

fig. S6. The ultralow density of the CNFAs. The weight measurement process for an ultralight CNFA (11.2 cm^{-3}) with a mass of 1.67 mg, which is corresponding to a density of 0.15 mg cm^{-3}.

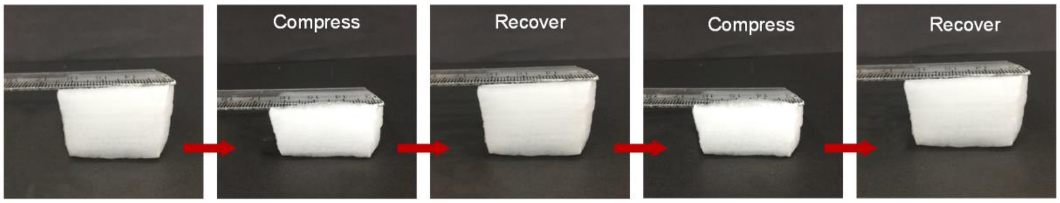

fig. S7. Compressibility of the CNFAs with a density of 0.15 mg cm^{-3}. Photographs showing the compression and recovery processes of a CNFA with density of 0.15 mg cm^{-3}.

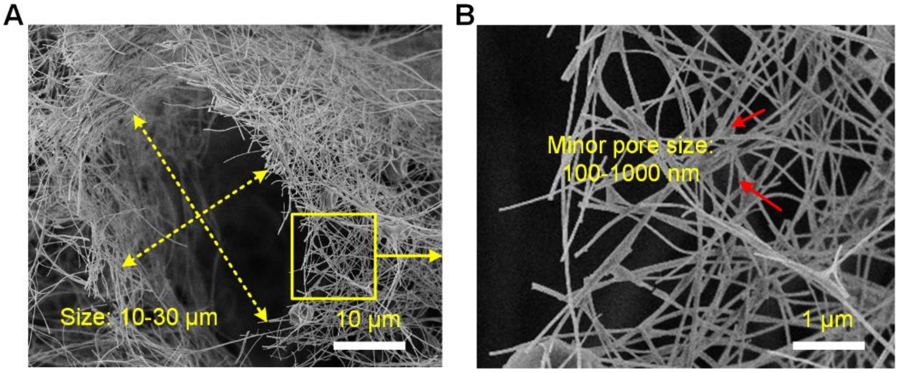

fig. S8. SEM images of the nanofibrous cell walls. SEM images showing the pore size of (**A**) a single cell and (**B**) the relevant minor pores on the nanofibrous cell walls.

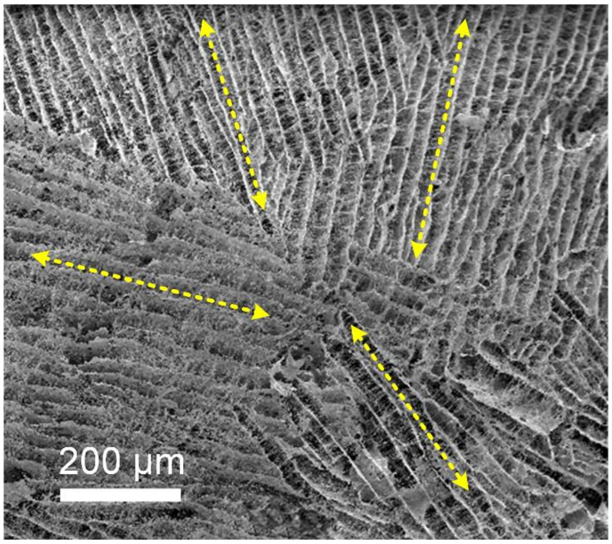

fig. S9. Micro-orientation and macro-isotropic structure of CNFAs. SEM image shows the micro-orientation and macro-isotropic cellular structure of the CNFAs.

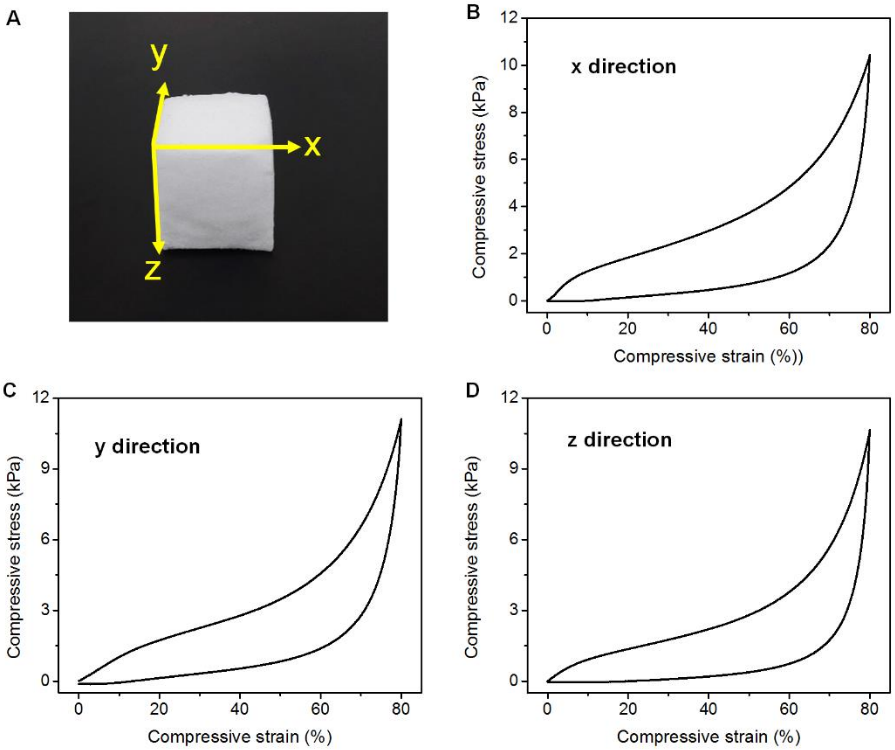

fig. S10. Mechanical properties of the CNFAs upon different orientation. (**A**) Three compressing direction (x, y, and z) on a cubic CNFA sample. (**B**-**D**) Compressive stress versus strain curves for CNFAs under three compressing direction.

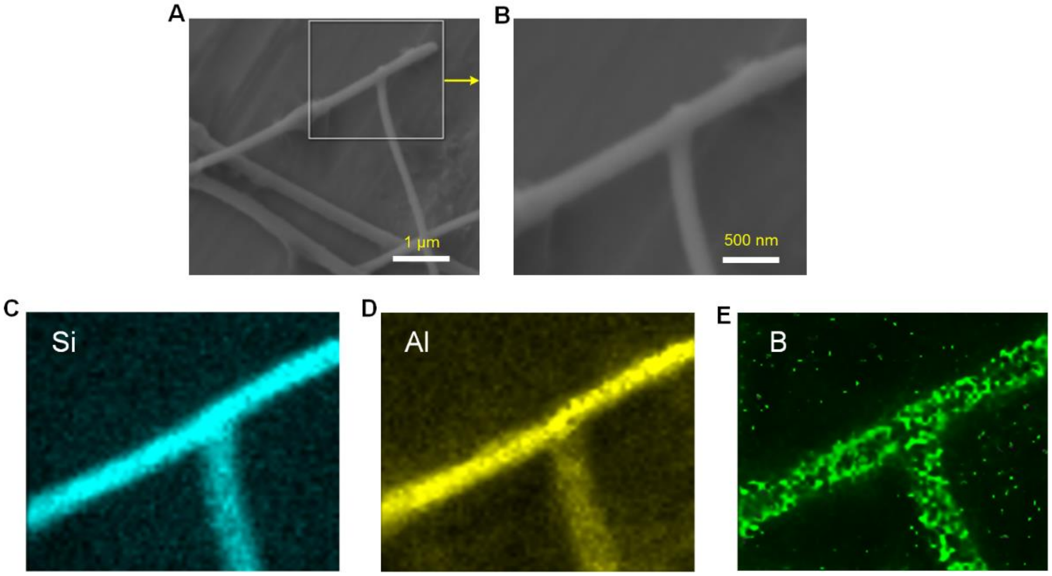

fig. S11. EDS mapping of junctions between nanofibers. STEM–EDS images of junctions between SiO_2 nanofibers with corresponding elemental mapping images of Si, Al, and B, respectively.

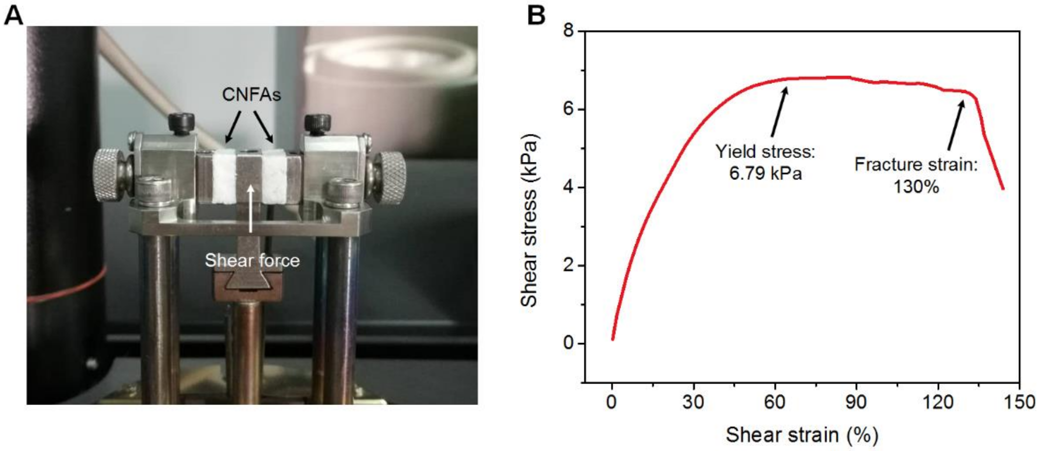

fig. S12. Shear mechanical properties of CNFAs. (**A**) The measurement of shear mechanical property was performed by using a TA-Q800 DMA instrument with a sandwich shear clamp. (**B**) Shear stress-strain curve for the CNFAs.

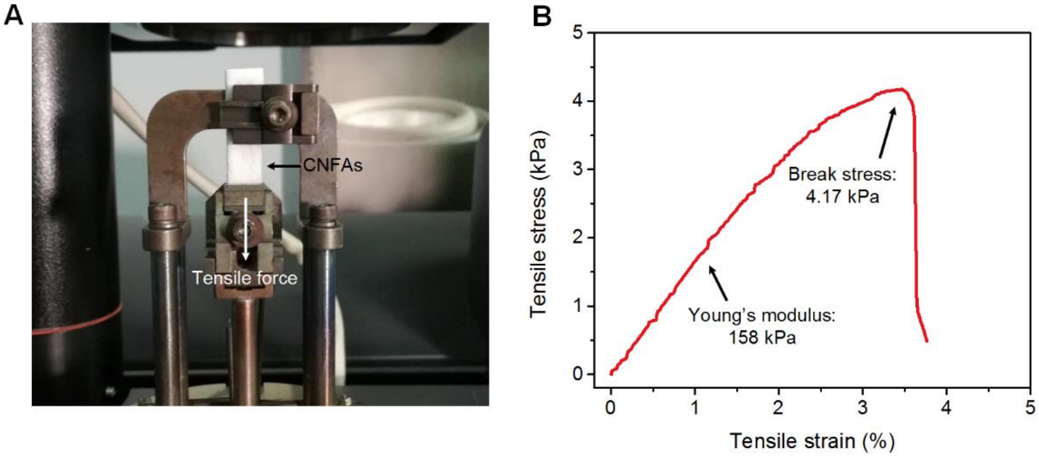

fig. S13. Tensile mechanical properties of CNFAs. (**A**) The measurement of tensile mechanical property was performed by using a TA-Q800 DMA instrument with a tensile clamp. (**B**) Tensile stress-strain curve for the CNFAs.

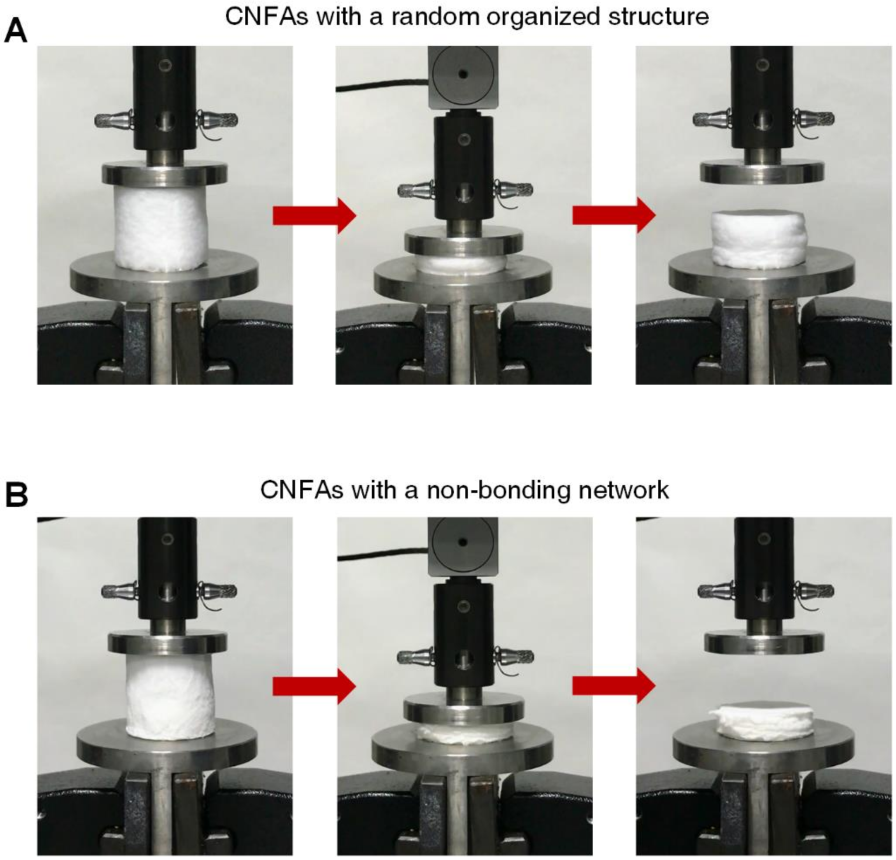

fig. S14. Elastic resilience of CNFAs with different structures. Optical photographs showing the compression and recovery test to 80% strain of (**A**) CNFAs with a random organized structure and (**B**) CNFAs with a non-bonding network.

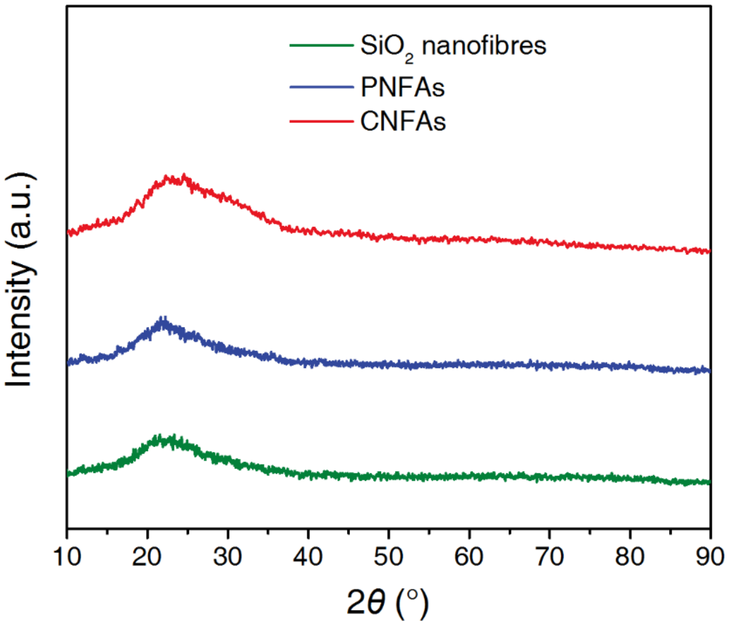

fig. S15. Amorphous character of the CNFAs. XRD patterns of the SiO$_2$ nanofibers, PNFAs, and CNFAs.

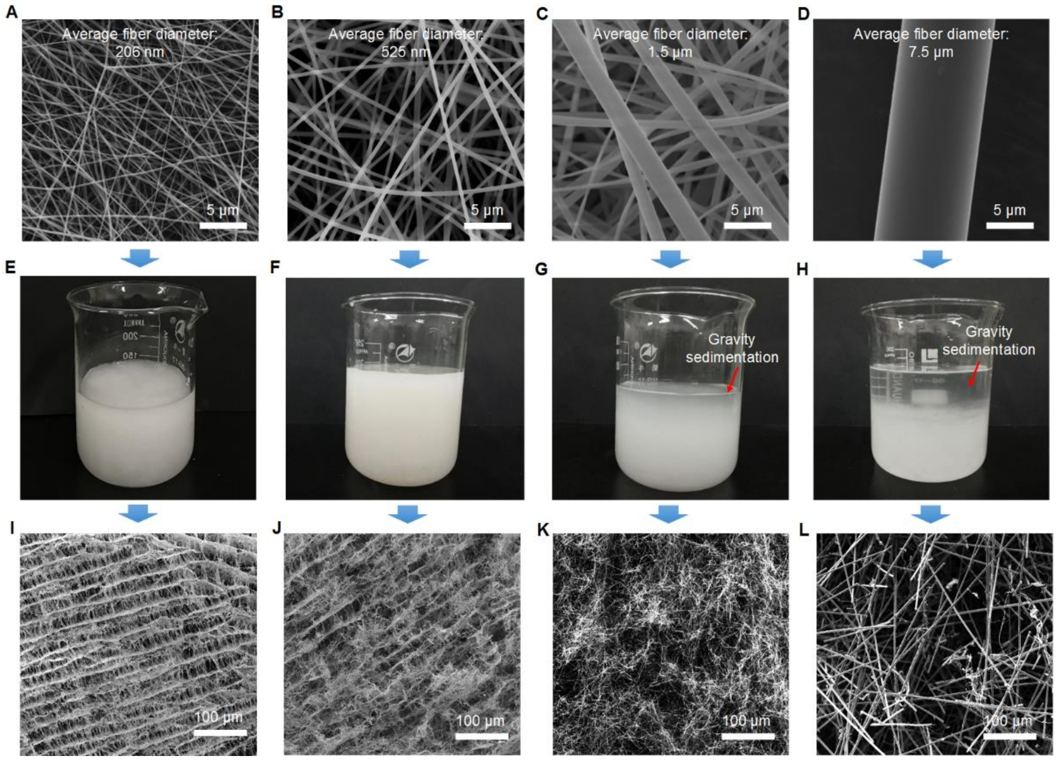

fig. S16. Effect of fiber diameter on the structure of CNFAs. (**A**-**C**) SEM images of the electrospun SiO$_2$ nanofibers. (**D**) SEM image of commercial SiO$_2$ microfibers. (**E**-**H**) Optical photographs of the homogenized fiber dispersions of the relevant SiO$_2$ fibers. (**I**-**H**) Microscopic structure of CNFAs fabricated from the relevant SiO$_2$ fibers.

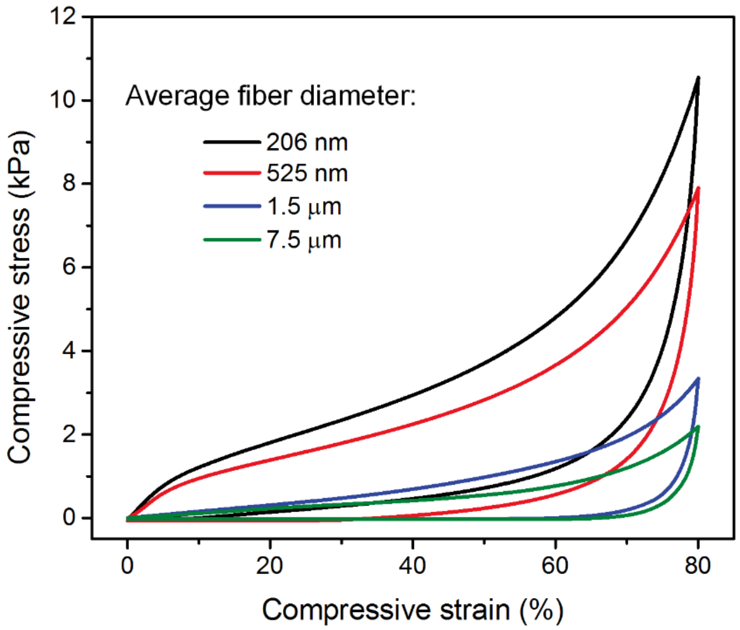

fig. S17. Effect of fiber diameter on the mechanical properties of CNFAs. Compressive stress-strain curves of CNFAs prepared from SiO_2 fibers with various average fiber diameters.

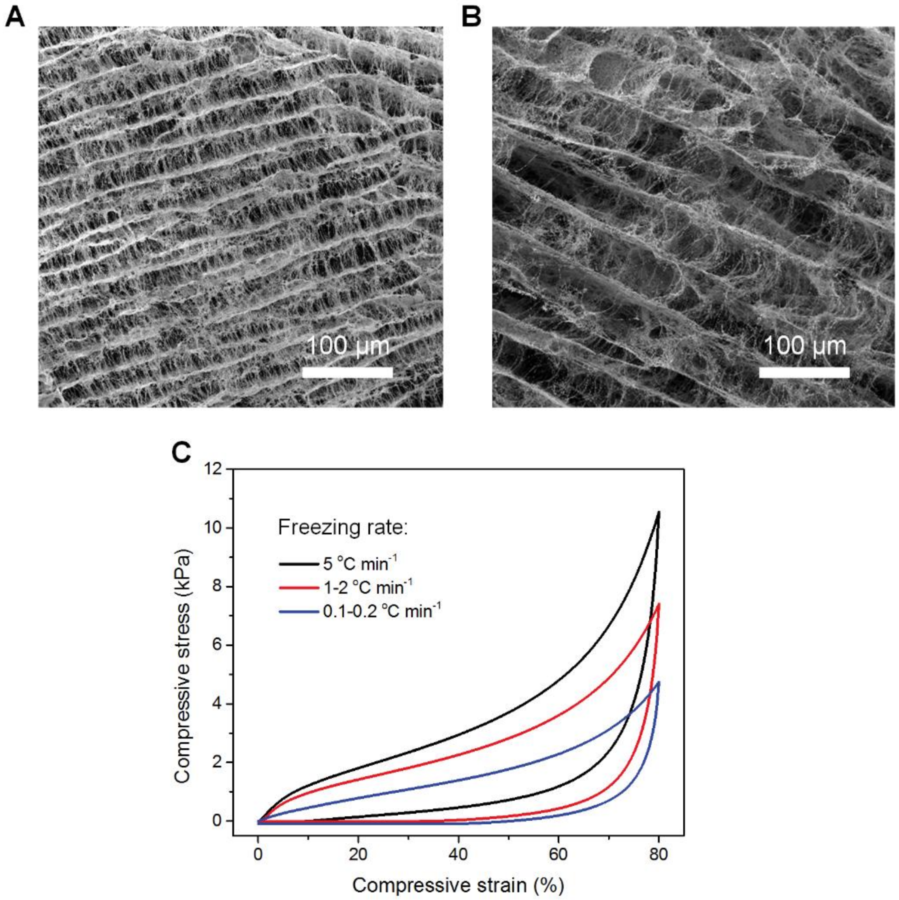

fig. S18. Effect of lamellar spacing on the structure and properties of CNFAs. SEM images of the CNFAs prepared with the freezing rate of (**A**) 5 °C min^{-1} and (**B**) 1 to 2 °C min^{-1}. (C) Compressive stress-strain curves of CNFAs prepared with various freezing rates.

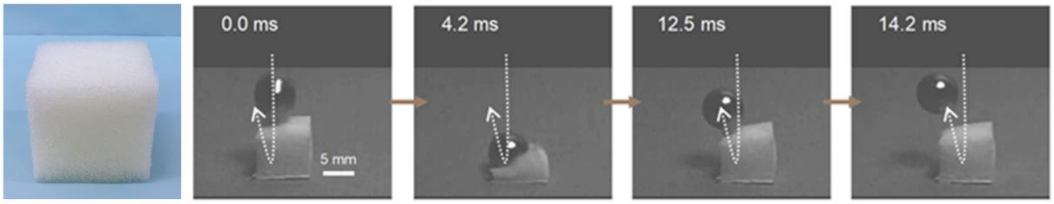

fig. S19. Elasticity of a PU foam. A set of real-time images showing that a selected PU elastic foam rebound a steel ball at high speed.

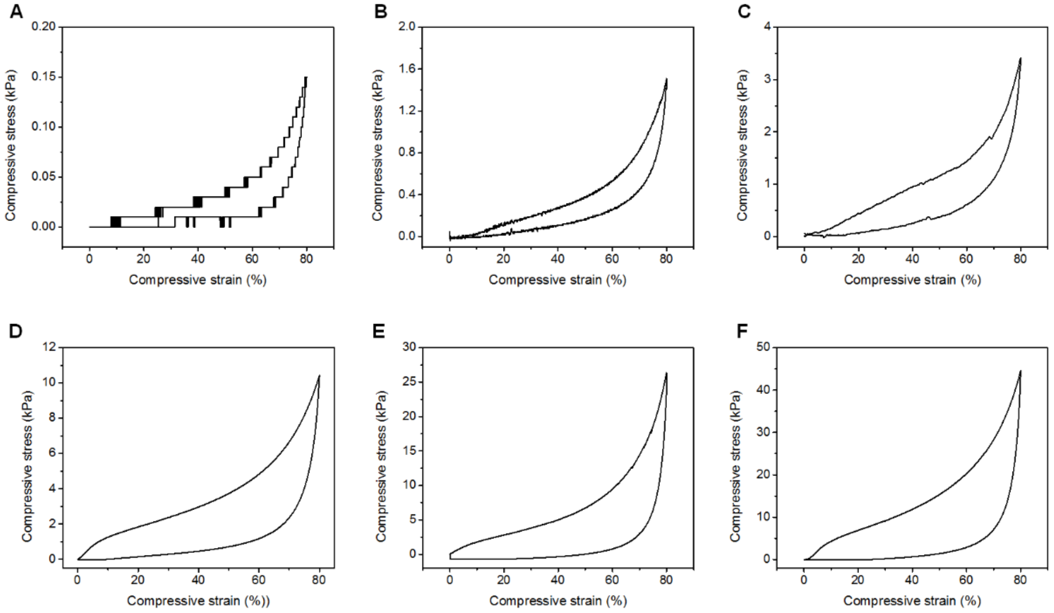

fig. S20. Elasticity of CNFAs with a wide range of densities. Compressive stress-strain curves of CNFAs with the densities of (**A**) 0.5, (**B**) 1, (**C**) 2, (**D**) 5, (**E**) 8, and (**F**) 10 mg cm^{-3}.

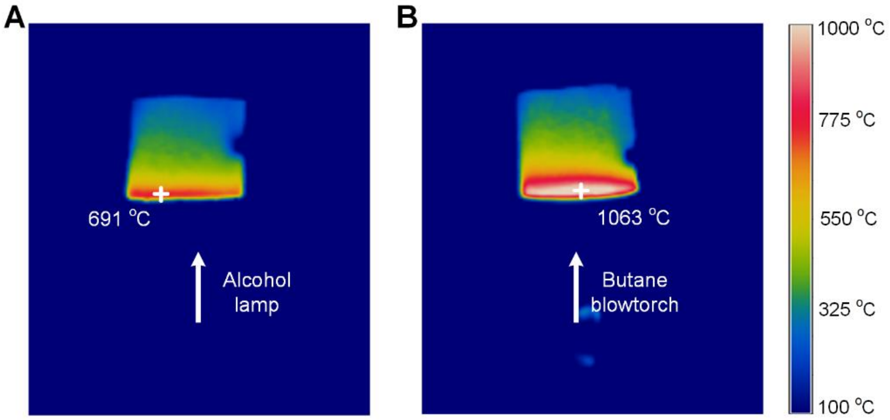

fig. S21. The temperature at the position of the CNFAs upon flames. Infrared images of CNFAs exposed to (**A**) an alcohol lamp and (**B**) a butane blowtorch.

table S1. The relevant densities and thermal conductivities of CNFAs and other insulation materials.

Materials	Density ($mg\ cm^{-3}$)	Thermal conductivity ($W\ m^{-1}\ K^{-1}$)
CNFAs	5	0.0255
Polyurethane foams	20–80	0.03–0.2
Polystyrene foams	40–80	0.025–0.15
Cork wood	100–400	0.045–0.15
Ceramic foams	200–500	0.08–0.2
Glass fiber felt	20–160	0.04–0.1
PP nonwovens	50–200	0.05–0.3
Cotton	100–400	0.07–0.1

Supplementary Methods

Preparation of SiO_2 nanofibers by sol-gel electrospinning.

The flexible SiO_2 nanofibers were prepared by a combination of electrospinning and sol-gel methods. The typical procedure is as briefly as follows: the silica precursor sol solution was prepared by stirring mixing tetraethyl orthosilicate (TEOS), H_3PO_4, and H_2O with a molar ratio of 1:0.01:11 at room temperature for 12 h. A 10 wt% polyvinyl alcohol (PVA, Mn = 86,000, Wako) aqueous solution was prepared by stirring dissolving 2 g of PVA powder in 18 g of water at 80 °C for 6 h. Then, the silica sol was added to PVA solution with a weight ratio of 1:1 and stirred for another 4 h. Following the electrospinning process was performed with an applied high voltage of 20 kV and a constant feed rate of 1 mL h^{-1}. The as-spun composite PVA/TEOS nanofibers with average fiber diameter of 352 nm were collected on the surface of a grounded aluminum foil-covered metallic rotating roller, as shown in fig. S1A. Finally, the composite nanofibers were dried at room temperature under vacuum for 2 h and calcined at 850 °C in air by gradually increasing the temperature at a heating rate of 5 °C min^{-1} to obtain pure SiO_2 nanofibers, which exhibited average fiber diameter of 206 nm, as shown in fig. S1B.

Homogenization of SiO_2 nanofibers.

The “homogenization” process refers to breaking the originally lamellar deposited SiO_2 nanofiber membranes into homogeneously-dispersed nanofiber dispersions. Because the electrospun nanofibers were closely packed and entangled, breaking this packed structure using traditional dispersion methods was difficult. Thus, we used a high-speed homogenizer (IKA T25) with an S25N-25F dispersing tool, which could generate an extremely strong shear force on the dispersoid. The operating speed in the experiment was 13,000 rpm, which could achieve a high shear rate (> 25 m s^{-1}). We also collected the SEM images of the homogenized fibers. The nanofiber dispersions were first diluted and cast onto an aluminum foil; they were then dried for the FE-SEM examination. As observed in fig. S3A and B, the nanofibers were well dispersed, with slight tangling; the fiber length ranged primarily from 50 to 200 μm, with an average length of 122 μm (fig. S3C).

Freezing and freeze-drying of nanofiber dispersions.

In the case of freezing procedure, the homogenized AlBSi/polyacrylamide/SiO_2 nanofiber dispersions were transferred to the desired mold, and then frozen in a dry ice/acetone bath (–77 °C). As shown in fig. S4A, the temperature curve exhibited two typical regimes with different slopes. The obvious slope change at 5 min indicated the completely frozen of water. Moreover, the estimated freezing rate was about 5 °C min^{-1} during the initial 5 min, which was significantly lower than that of vitrification, indicating the crystallization of water. The following freeze-drying process was performed using a programmable freeze-drying system with gradually increasing temperature. As shown in fig. S4B, both the temperature and weight curves exhibited two obvious regimes with different slopes, which were corresponding to the sublimation and desorption drying processes. It was also founded that 90 wt% of the ice crystals were sublimated in the first 8 h, and the remnant hydrated water was removed within an addition 4 h of desorption.

Measurement of the density and porosity of the CNFAs.

The density of the CNFAs mentioned in this manuscript was the “apparent density” rather than the absolute density, which was measured on the basis of the ISO 845:2006 standard: Cellular plastics and rubbers—Determination of apparent density. This standard is the current standard practice for measuring the density of cellular materials. The density of the aerogels was calculated using the weight of the solid contents, without including the weight of air entrapped in the pores, according to the following formula

$$Apparent\ density = \frac{Mass\ of\ solid\ constituents}{Volume\ of\ test\ sample}$$

Because the samples were weighed in air, the weight of air was automatically eliminated. On the basis of this formula, the theoretical apparent density of air should be 0 mg cm^{-3}; thus, although the apparent density of the CNFAs was 0.15 mg cm^{-3}, it is still higher than that of air.

The free volume (porosity) of CNFAs was determined based on the standard practice for cellular materials using the following formula

$$\eta = \frac{V_0 - m/\rho}{V_0} \times 100\%$$

where η is the porosity, V_0 is the volume of the cellular materials, m is the mass of the solid constituents, and ρ is the density of solid constituents. In the case of the CNFAs with a low density of 0.15 mg cm^{-3}, the solid constituents in the aerogels are the SiO_2 nanofibers and AlBSi ceramics, which have similar density of about 2.2 g cm^{-3}. Thus the calculated $\eta = (1 – 0.00015/2.2) \times 100\% = 99.993\%$.

Calculation of the compression work

The work mentioned in the manuscript is the specific work of compression, which is defined as the work performed for generating compression deformation per unit volume, as determined by the following formula

$$W = \int_{\varepsilon 1}^{\varepsilon 2} \sigma d\varepsilon$$

where W is the specific work, ε_1 and ε_2 are the initial and final compressive strain, respectively, and σ is the compressive stress. Thus, the compression and recovery work were calculated by integrating the relevant stress-strain curves.

Supplementary Discussions

Elastic resilience of CNFAs with a random structure or a non-bonding network.

We have indicated in the main article that both the ordered cellular structure and well-bonded nanofibers contributed to the elasticity of the CNFAs. To further verify this, we prepared the CNFAs with a random organized structure or a non-bonding network fabricated from the same precursor. As elaborated on the main article, the cellular structure of the CNFAs was a direct replica of the solidified lamellar ice crystals during freezing. Generally, the size of the ice crystals was regulated by the freezing rate, and a slower freezing rate led to the formation of larger and irregular ice crystals. The normal sample frozen by a dry ice/acetone bath (–77 °C) with a high freezing rate of 5 °C min^{-1} resulted in the CNFAs with the cell size of 10-30 μm. To obtain the random organized cells, we frozen the nanofiber dispersions by an common refrigerator with a very low freezing rate of 0.1 to 0.2 °C min^{-1}, which led to irregular cells and even big cracks with size over 1 mm in the CNFAs. As shown in fig. S14A, the relevant CNFAs exhibited large plastic deformation of > 30% upon 80% compressive strain, which indicated that the cellular networks cannot recover their original shape. In the case of the non-bonding network, we prepared the CNFAs from the same precursor but without adding AlBSi crosslinking matrices, which means that the SiO_2 nanofibers cannot bonded with each other. As shown in fig. S14B, nearly no recovery was observed for the relevant CNFAs after 80% compressive strain, indicating that the cellular networks were completely collapsed.

Shear and tensile mechanical properties of the CNFAs

The measurement of the shear mechanical property was performed using a TA-Q800 DMA instrument with a sandwich shear clamp, as shown in fig. S12A. The shear stress-strain curve was measured at a maximum strain of 200% and with a strain rate of 50% min^{-1}. As observed in fig. S12B, the shear stress-strain curve for the CNFAs (ρ = 5 mg cm^{-3}) exhibited three typical regimes under increasing strain. The first regime was an elastic deformation stage at strain < 60%; in this regime, the stress increased dramatically with increasing strain. The second regime was a large plastic deformation plateau after the yield point, with a strain of 60–130%; the stress nearly remained constant. The last stage occurred after the ultimate stress, with strain > 130%; in this regime, the stress rapidly decrease due to the appearance of cracks in the samples. The maximum shear stress of the CNFAs was 6.79 kPa, with a large fracture shear strain of 130%, indicating the robust resistance to shear strain.

The tensile tests were performed on a TA-Q800 DMA instrument with a tensile clamp, as shown in Supplementary fig. S13A. Rectangular samples with thicknesses of 3 mm were used, and the tensile loading rate was 25% min^{-1}. The tensile stress-strain curve of the CNFAs (ρ = 5 mg cm^{-3}) presented in fig. S13B exhibited a tensile behavior typically observed in open-cell foams. As the strain increased, the stress first increased linearly with a robust Young's modulus of 158 kPa, and fracture occurred immediately after the stress reached its maximum yield value of 4.17 kPa.

Mechanical properties on different orientations

The formation of the cellular structure could be attributed to the phase separation induced by the crystallization of water. The lamellar ice crystals grow from the initial crystal nucleus, thus, the growth direction would orient in a limited micro-scale which was caused by one crystal nucleus or neighboring nucleuses. However, the generation of the crystal nucleus was randomly distributed in the whole sample, which caused the isotropic growth of the ice crystal in the macro-scale. Therefore, the orientation of the cellular structure is limited in the small area, the bulk cellular structure is isotropic, as shown in fig. S9. Moreover, we have measured the mechanical properties of a cubic CNFAs through three direction (x, y, and z), as shown in fig. S10A. The resulting stress-strain curves under different directions exhibit very similar behavior with each other (fig. S10B-D), indicating the isotropic mechanical properties of the CNFAs. This result is also agree with the above structure analysis.

Effect of the fiber diameter on the mechanical properties of CNFAs

In the case of nanofiber diameter, generally, the available diameter range of electrospun SiO_2 nanofibers is from 200 to 2000 nm by changing the fabrication parameters. The SiO_2 nanofibers (206 nm) used in this work are almost the thinnest available SiO_2 nanofibers (fig. S16A). We also fabricated electrospun SiO_2 nanofibers with larger fiber diameters of 525 nm and 1.5 μm (fig. S16B and C). To further investigate the diameter effect, commercial SiO_2 microfibers (diameter of 7.5μm) prepared by melt-spinning were also used for comparison (fig. S16D). Subsequently, all of these SiO_2 fibers were homogenized with AlBSi sol under identical conditions. As shown in fig. S16E-H, the fiber diameter significantly affect the homogeneity of the resulting fiber dispersions. Obvious gravity sedimentation were observed in the dispersion with larger fiber diameter, which could be attributed to the higher weight of a single fiber. Consequently, the cellular structure of the resulting CNFAs were also greatly affect by the fiber diameter. As shown in fig. S16I-L, with the increasing of fiber diameter, the organized "lamellar-cell geometry" were gradually disappeared, the CNFAs with fiber diameters of 1.5 and 7.5 μm nearly showed random porous structure. Moreover, it should be noted that the surface wrapped AlBSi crosslinking layer was also unable to provide stable bonding for SiO_2 fibers with larger diameter because of the relatively thin thickness (due to the same concentration of AlBSi sol). Finally, because both the cellular structure and crosslinking (the two critical factors for elasticity) were significantly affected by the fiber diameter, the resulting mechanical properties of the CNFAs were certainly affected. As shown in fig. S17, the CNFAs with fiber diameter of 525 nm exhibited a lower stress of 7.9 kPa at 80% strain than that of typical CNFAs with fiber diameter of 206 nm. Moreover, very low stress (<3 kPa) and poor elastic recovery (<20%) were observed for the relevant CNFAs with larger fiber diameter (1.5 and 7.5 μm) after 80% compressive strain, indicating that the cellular networks were largely collapsed upon compression.

Effect of the lamellar spacing on the mechanical properties of CNFAs

In the case of lamellar spacing, as elaborated on the main article, the lamellar cellular structure of the CNFAs was a direct replica of the solidified lamellar ice crystals during freezing, thus, the size of the lamellar spacing was dedicated by the size of the ice crystals. Generally, the size of the ice crystals was regulated by the freezing rate, and a slower freezing rate led to the formation of larger and irregular ice crystals. The normal sample frozen by a dry ice/acetone bath (–77 °C) with a high freezing rate of 5 °C min^{-1} resulted in the CNFAs with the lamellar spacing of 10-30 μm (fig. S18A). Meanwhile, the sample frozen by a bath with a lower freezing rate of 1 to 2 °C min^{-1} resulted in the CNFAs with larger lamellar spacing of 50-100 μm (fig. S18B). An even lower freezing rate of 0.1 to °C min^{-1} using a common refrigerator might led to irregular cells and even big cracks with spacing size over 1 mm. Moreover, we also measured the compressive mechanical properties of the CNFAs prepared with various freezing rates. As shown in fig. S18C, the CNFAs with freezing rate of 1 to 2 °C min^{-1} exhibited a lower stress of 7.4 kPa at 80% strain than that of typical CNFAs. The CNFAs with freezing rate of 0.1 to 0.2 °C min^{-1} (largest lamellar spacing) showed lowest stress of 4.6 kPa and a large plastic deformation of > 30% upon 80% compressive strain (see also fig. S14A), which indicated that the cellular networks cannot recover their original shape.